JOURNAL OF GEOPHYSICAL RESEARCH, VOL. 115, C07010, doi:10.1029/2009JC005966, 2010

Nares Strait hydrography and salinity field from a 3-year moored array

B. Rabe,[1] A. Münchow,[1] H. L. Johnson,[2] and H. Melling[3]

Received 4 November 2009; revised 2 February 2010; accepted 1 March 2010; published 17 July 2010.

[1] Nares Strait to the west of Greenland facilitates the exchange of heat and freshwater between the Arctic and Atlantic Oceans. This study focuses on salinity, temperature, and density measurements from Nares Strait from a mooring array deployed from 2003 to 2006. Innovative moorings requiring novel analysis methods measured seawater properties near 80.5°N, at spacing sufficient to resolve the internal Rossby deformation radius. The 3-year mean geostrophic velocity has a surface-intensified southward flow of 0.20 m s^{-1} against the western side of the strait and a secondary core flowing southward at 0.14 m s^{-1} in the middle of the strait. Data show warm salty water on the Greenland side and cold fresher water on the Ellesmere Island side, especially in the top layers. There was a clear difference in hydrographic structure between times when sea ice was drifting and when it was land fast. Ice was drifting in late summer, fall, and early winter with a strong surface-intensified geostrophic flow in the middle of the strait. Ice was land fast in late winter, spring, and early summer, when there was a subsurface core of strong geostrophic flow adjacent to the western side of the strait. Salinity variations of about 2 psu in time and space reflect a variable freshwater outflow from the Arctic Ocean. One particularly strong pulse occurred at the end of July 2005. For several days, steeply sloping isohalines indicated strong geostrophic flow down the middle of the strait coinciding with an amplified ice export from the Arctic due to strong southward winds.

Citation: Rabe, B., A. Münchow, H. L. Johnson, and H. Melling (2010), Nares Strait hydrography and salinity field from a 3-year moored array, *J. Geophys. Res.*, *115*, C07010, doi:10.1029/2009JC005966.

1. Introduction

[2] The heat and freshwater budgets of the Arctic Ocean play an important role in the global climate system. Freshwater fluxes toward the North Atlantic occur through the shallow straits of the Canadian Arctic Archipelago (hereafter CAA) and deep Fram Strait [*Aagaard and Carmack*, 1989]. A simple ocean-sea-ice model suggests that the ocean transport of freshwater through Fram Strait is about 60% of that through the CAA [*Steele et al.*, 1996] but contributions from ice are small in the CAA due to the presence of land-fast ice [*Prinsenberg and Bennett*, 1989; *Melling et al.*, 2008]. These freshwater fluxes into the Labrador and Greenland Seas are a source of buoyancy that stratifies the water column and, if it reaches deep convection regions, reduces deep convection.

[3] Atlantic water flows into the Arctic Ocean through Fram Strait and Barents Sea [*Fahrbach et al.*, 2001; *Schauer et al.*, 2002] while Pacific Water enters through Bering Strait [*Coachman and Aagaard*, 1966; *Woodgate and Aagaard*, 2005]. Assemblies of these water masses are augmented by runoff from the Eurasian and American continents and return to the Atlantic via Fram Strait and the CAA. Waters are modified in transit, but their origins remain clear.

[4] Salinity shows temporal and spatial variability over a wide range of scales in the CAA and adjacent oceans. For example, the "Great Salinity Anomaly" was a freshwater anomaly that traveled throughout the North Atlantic between 1968 and 1982. It originated from Fram Strait, traveled southward in the East Greenland Current, and freshened the central Labrador Sea [*Dickson et al.*, 1988]. Numerical models such as those of *Goosse et al.* [1997], *Tang et al.* [1999], *Wadley and Bigg* [2002] simulate the connection between changes in freshwater fluxes (for example, caused by the "Great Salinity Anomaly") and convection, but these spatially coarse resolution models do not represent the coastal and rim-current systems in the Greenland and Labrador Seas [*Sutherland and Pickart*, 2008]. *Koenigk et al.* [2007] use 20th-century and Intergovernmental Panel on Climate Change scenario runs for an investigation of the changing freshwater export out of the Arctic Ocean using a model with grid spacing of about 15 km around Greenland. They suggest an increase in the liquid freshwater outflow through the whole CAA from about 60 mSv (Sv = 10^6 m^3 s^{-1}) to more than

[1]College of Earth, Ocean, and Environment, University of Delaware, Newark, Delaware, USA.
[2]Department of Earth Sciences, University of Oxford, Oxford, UK.
[3]Institute of Ocean Sciences, Sidney, British Columbia, Canada.

0148-0227/10/2009JC005966

100 mSv by 2100 without distinguishing between different straits in the CAA. Obtaining reliable volume and freshwater flux estimates and describing the hydrography in Nares Strait as part of the CAA is particularly important; longer term measurements did not exist in Nares Strait (one of the main channels in the CAA) as they do, for example, in Lancaster Sound [*Prinsenberg and Hamilton*, 2005]. Flux estimates may be used to monitor change and to constrain the models used to make climate predictions. Note, however, that few of the current generation of climate models allow any flow of water through the channels of the CAA, with unknown consequences for projections.

[5] Nares Strait to the west of Greenland facilitates a total southward volume flux estimated to be 0.57 ± 0.09 Sv [*Münchow and Melling*, 2008], 0.7 Sv [*Sadler*, 1976], and 0.8 ± 0.3 Sv [*Münchow et al.*, 2006]. This compares to a net yearly southward transport in Fram Strait of 2 ± 2 to 4 ± 2 Sv [*Schauer et al.*, 2004]. The net southward Atlantic Water flux in Nares Strait is about 0.59 ± 0.13 Sv and the net southward Pacific Water flux is about 0.32 ± 0.04 Sv [*Münchow et al.*, 2007]. Ice flux through Nares Strait is small as ice is land fast during most of the year. Unpredictable ice conditions in the short summer season have resulted in only limited expeditions to this area in the past.

[6] First studies in Nares Strait include *Sadler* [1976], who interpreted data from a 40-day long data set of current measurements, and *Bourke et al.* [1989], who evaluated temperature and salinity during one summer season. *Münchow et al.* [2006] used data from a synoptic 2-day Acoustic Doppler Current Profiler (ADCP) survey to evaluate fluxes. The first longer term measurements were conducted as part of the Canadian Archipelago Throughflow Study from 2003 to 2006. This project resulted in 3-year data sets from ADCP moorings with first results regarding interannual to tidal variability and forcing published by *Münchow and Melling* [2008]. The conductivity, temperature, and pressure data set collected during the project is evaluated here with regard to hydrography and salinity variability. Also included in the project was an atmospheric modeling component [*Samelson and Barbour*, 2008].

[7] The width of a baroclinic flow in geostrophic balance scales with the internal Rossby deformation radius:

$$L_D = \frac{(g' D_0)^{1/2}}{f} \tag{1}$$

with $g' = \frac{\Delta\rho g}{\rho_0}$ as the reduced gravity, ρ_0 the mean density, $\Delta\rho$ the density difference, g the gravitational constant, f the Coriolis parameter, and D_0 the vertical scale of motion. This is the fundamental spatial scale of motion in the CAA [*LeBlond*, 1980] and is about 10 km for Nares Strait [*Münchow et al.*, 2006], significantly less than the width of the strait.

[8] This study introduces the novel 3-year data set of temperature, conductivity, and pressure records (section 2) from the moored array in Nares Strait that resolves the density and thus geostrophic velocity field at the scale of the internal Rossby deformation radius. The year-round presence of ice and icebergs poses a constant threat to all moored equipment deployed in these waters. These challenges require both unique mooring design and data processing. Therefore, we discuss our nonstandard methods in detail in section 3 and Appendix A. Section 4 then describes the 3-year mean hydrography and water masses from these moored records and compares them with snapshots of more traditional survey data. Salinity variability in space and time, and a large Arctic freshwater incursion event, are described in sections 5 and 6, respectively. The results from this study are discussed in section 7, and section 8 contains concluding remarks. This paper focuses on characterizing the 3-year mean and the variability seen in the salinity field; a second paper in preparation ("Geostrophic ocean currents and freshwater fluxes across the Canadian Polar Shelf via Nares Strait" by Rabe et al.) will explore in more detail the physics governing variability in the flow.

2. Study Area and Data Sources

[9] The Canadian Archipelago lies on the Canadian polar shelf, amid a network of straits and basins that provide pathways for flow between the Arctic Ocean and the North Atlantic. This study focuses on Nares Strait in the northeast CAA between Ellesmere Island and Greenland. The channel is less than 400 m deep and 38 km wide and comprises, from north to south, Robeson Channel, Hall Basin, Kennedy Channel, Kane Basin, and Smith Sound (Figure 1a). Conductivity-temperature (CT) mooring strings were deployed across the strait in Kennedy Channel at about 80.5°N, about 50 km north of the 230 m deep sill. The CT moorings were about 5 km apart. All instruments were deployed in August 2003 from USCGC *Healy* and recovered in 2006 from CCGS *Henry Larsen*. Specifically, we recovered 24 SeaBird SBE37SM Microcats (hereafter CT instruments) from six moorings; two moorings were lost (see Table 1 and Figure 1b for mooring locations in the strait). Additional recovered ADCP moorings are discussed by *Münchow and Melling* [2008] and included a further four CT instruments.

[10] The CT recorders were supported on taut-line moorings at four depths, nominally 30, 80, 130, and 200 m (Figure 2). Actual depths when drawdown was zero are listed in Table 1. One acoustic transponder release was attached above the anchor. The buoyancy above depths of 200 m on each mooring was small, so the top of the mooring pulled down appreciably in strong current. The mooring relied on strings of small plastic floats for buoyancy at upper levels, instead of conventional large spherical floats. The sensitivity to current was deliberate: since icebergs sweep larger volumes per unit time in strong current, pull-down in such conditions reduces the likelihood of strikes. This design proved essential for the survival of the moorings during their 3-year deployment (only two moorings were lost, both in shallow locations). For example, during its first year of deployment one instrument was pulled down from its nominal 30 m location to below a depth of 200 m by a passing iceberg. The slender mooring design ensured that no damage occurred during this iceberg encounter and that data collection continued for another 2 years. The "normal" drawdown of the top-most instrument by tidal current was about 50 m. Twice a day near slack tide, when the mooring straightened up, observations were acquired within 30 m of the surface. This novel mooring design, which encouraged large vertical movement of the CT instruments, introduces new challenges to the processing of time-series data.

[11] To facilitate the processing and analysis of data, about half of the CT instruments were equipped with pressure

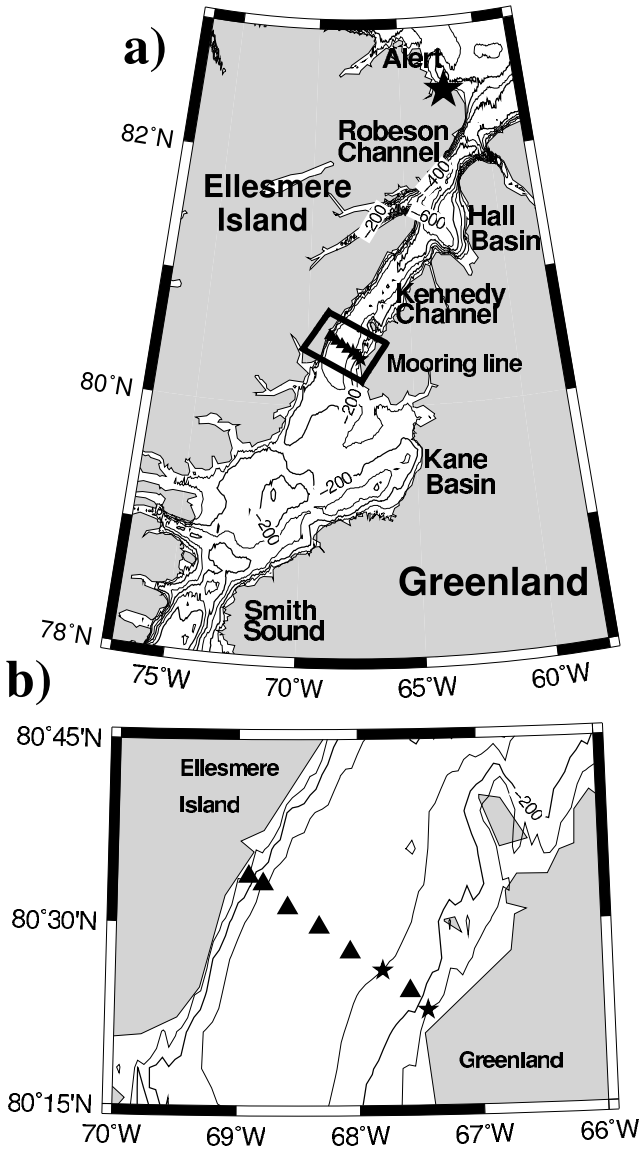

Figure 1. Study area. (a) Nares Strait bottom topography with thick black line of triangles denoting CT mooring locations. Greenland lies to the east of Nares Strait. Robeson Channel is in the northern part of the strait, Hall Basin connects to Kennedy Channel at roughly 81°N, and Kane Basin connects to Smith Sound to the south with a sill depth of 230 m. The big star shows Alert in northeastern Ellesmere Island. The black box is the area zoomed in for Figure 1b with more detail on exact mooring locations. (b) Mooring line across Nares Strait with triangles denoting recovered CT mooring strings and stars denoting lost CT mooring strings.

sensors to measure depth. Figure 3 illustrates the record-mean position of each instrument within the cross section and shows the naming convention of moorings. Individual CTD sensors were placed near the top (nominal 30 m depth) and bottom (nominal 200 m depth) of the array of sensors, bracketing two CT instruments without pressure sensors placed at nominal depths of 80 and 130 m (Figure 2).

[12] The instruments were factory calibrated prior to deployment and checked for calibration issues after recovery. Biological fouling was minimal on all instruments. The sampling interval was 15 min. All instruments returned a gap-free 3-year conductivity and temperature record, but the pressure record at one instrument terminated after 500 days. We adjusted the records of each instrument for (a) a generally small clock drift (<3 min per year), (b) a small number of spikes (<0.01%), and (c) a recorded pressure drift. The latter was accomplished by comparing in-air pressure readings at the beginning and the end of the record. Measured pressures were not corrected for variations in tide and sea level atmospheric pressure, which in combination spanned a full range of values of 5 dbar with a standard deviation of 0.9 dbar during the period of recording estimated from pressure measured 3 m above the seabed at ADCP mooring KS10.

3. Methods

[13] Currents associated with the barotropic tide in Nares Strait cause most of the observed drawdown of instruments on moorings. These currents are both deterministic and predictable [*Padman and Erofeeva*, 2004; *Münchow et al.*, 2006; *Münchow and Melling*, 2008]. *Münchow and Melling* [2008] find from a 3-year time series of vertically averaged along-channel currents that 66.4% and 26.3% of the total variance reside within the semidiurnal and diurnal bands, respectively. For the dominant M_2 tidal currents the flow along the major axis (along-channel) reaches 21.2 ± 0.1 cm s^{-1} and K_1 reaches 13.0 ± 0.7 cm s^{-1}. The tides therefore lend support to the use of linear system analysis in deconvolving the effect of drawdown on time-series data.

[14] First, pressure is interpolated between CT instruments at nominal depths of 30 and 200 m to the location of the two instruments without pressure sensors at nominal depths of 80 and 130 m. A linear variation of pressure along the mooring line is assumed. Details about the pressure interpolation can be found in Appendix A1.

[15] Next, the effect of mooring motion and tides need to be minimized. We used a linear system analysis that is described in detail in Appendix A2. The analysis acts as a pre-processing step before applying filters also described in Appendix A3. The final time series are low-pass-filtered time series of temperature and salinity that are incoherent with cyclical vertical movement of CT sensors in response to varying tidal current.

[16] We define the along- and across-channel directions as x and y coordinates, respectively; therefore, u is the along-channel velocity (positive southward) and v the across-channel velocity (positive eastward). For thermal wind we use the depth z_0 = 200 m as a level of known motion to estimate the mean geostrophic velocity for our mooring section. We use the mean of available ADCP data from moorings KS02, KS10, and KS12 at 200 m (discussed in *Münchow and Melling* [2008]), that is, $u_0(y, z_0)$ = 0.04 m s^{-1}. The 3-year mean velocity is uniform across the strait at this depth.

[17] For the analysis of salinity variability we will use empirical orthogonal functions (EOF) to decompose observations into mutually uncorrelated (orthogonal) modes of var-

Table 1. CT Instruments: Mooring Name, Location (Latitude, Longitude), Record Length (Days), Depths With Zero Drawdown, and Type of CT Instruments

Mooring	Latitude	Longitude	Record length (days)	Depths and type of instruments (m)
KS01	80°33.4702′N	68°54.4556′W	1108	30[a] 80 130 200[a]
KS03	80°32.6972′N	68°47.3071′W	1104	29[a] 79[a] 129 199[a,b]
KS05	80°31.1389′N	68°34.8083′W	1104	27[a] 77 127 197[a]
KS07	80°29.3721′N	68°19.4548′W	1105	32[a] 82 132 202[a]
KS09	80°27.3490′N	68°03.8391′W	1104	38[a] 88 138 208[a]
KS11	80°25.6500′N	67°47.8325′W	Not recovered	17[a] 67 117 187[a]
KS13	80°23.8010′N	67°34.5747′W	1106	32[a] 82 132 202[a]
KS15	80°22.5009′N	67°25.8209′W	Not recovered	47[a] 97 106[a]

[a]Pressure sensor.
[b]Pressure sensor malfunction after 500 days.

iability. An extensive description of EOFs can be found in Appendix B.

4. Mean Hydrography and Water Masses

[18] In order to evaluate different water masses in Nares Strait, we present temperature-salinity correlations in Figure 4 using the 3-year mean of the time series from each instrument at each mooring (black triangles) and compare them to CTD data from a section across Kennedy Channel during 2007 for the same depth range. Note that CTD data were obtained in summer only and that ice conditions prevented us from taking measurements within 5 km of Ellesmere Island. For salinities larger than 33 psu, the mean water mass properties match the instantaneous CTD observations well since water masses at depth (warm and salty conditions) show less variability (see the sections of standard deviation of salinity and temperature in Figure 5). These warm and salty subsurface waters below depths of about 80 m contain waters of Atlantic origin [*Münchow et al.*, 2006]. Considerable scatter exists for the cooler and fresher waters of the upper layer that contains local ice melt and lies closer to the freezing point. The local ice melt, leading to salinity variations in the top layers, occurs only during the drift ice season. The 3-year mean from CT instruments captures both drift and fast-ice conditions and we would therefore not expect it to agree closely with a summer snapshot measured by CTD. The 3-year mean is representative of the lower layers throughout the year due to low variability but not representative of upper layer conditions in any particular season.

[19] Figure 5 shows the same 3-year average hydrographic conditions plotted as sections across southern Kennedy Channel. Again, we distinguish a surface layer of cold and freshwater that becomes warmer and saltier both with depth and toward Greenland. Temperatures drop almost to the freezing point at a salinity of 32 psu. Below 100 m depth we find warm and salty waters of Atlantic origin that are most pronounced on the Greenland side with temperatures of up to almost 0°C and salinities as high as 34.5 psu in the 3-year mean. Temperature has little influence on density at these low temperatures. The across-channel density gradient in Nares Strait is caused by fresher waters in the west and saltier waters at depth in the east. Isopycnals thus slope upward toward Greenland, which implies an across-channel baroclinic pressure gradient that, if geostrophically balanced, corresponds to a southward flow of up to 0.14 m s^{-1} near the center of the channel at the surface.

[20] Standard deviations about these mean properties demonstrate temporal variability that varies substantially across the strait (Figure 5). Small standard deviations for salinity occur at depth and near the channel center where they are generally less that 0.2 psu. Water properties below 150 m are similar across the section and, as will become clear in the next section, are largely independent of seasonal changes such as the presence of ice. We find the highest standard deviation of almost 0.5 psu in the surface layer off Ellesmere Island where we find the freshest water, while off Greenland the standard deviation reaches 0.3 psu. A minimum of salinity variability occurs near the channel center where the slopes of isopycnal surfaces are large. This suggests a steady geostrophic flow and we will argue below that this is the location of strong southward flow. For temperature the largest standard deviations are about 0.2°C both near Greenland and Ellesmere Island. The pattern of variability for density mimics salinity since density follows salinity at low temperatures.

5. Salinity Variability

[21] We performed an EOF analysis of the salinity data from our 24 time series across Kennedy Channel to investigate dominant in-phase patterns of covariability in salinity. We find that the first two modes explain almost 3/4 of the total variance contained in the 24 time series. Specifically, mode one explains 54% and mode two explains 19% of the total variance. The principal component time series $a_1(t_k)$ and $a_2(t_k)$ (Figure 6) are normalized so that they always have a zero mean and a variance of 1. This treatment aids the interpretation of the spatial patterns $\phi_1(\vec{x}_i)$ and $\phi_2(\vec{x}_i)$ (Figures 7 and 8), because these now are in practical salinity units. It is important to recall that EOFs describe only statistical variances about a mean that is not part of the analysis. Therefore, each mode n modifies the mean $\overline{S}(\vec{x}_i)$ by either adding or subtracting its pattern $S_n(\vec{x}_i)$ to the mean pattern [*Harms and Winant*, 1998; *Münchow and Chant*, 2000; *Pickart*, 2004].

[22] Figures 6a and 6b show the time series $a_1(t_k)$ and $a_2(t_k)$ representing an amplification factor in time of the time-invariant patterns shown in Figures 7 and 8 as the positive $[\overline{S}(\vec{x}_i) + S_n(\vec{x}_i)]$ and negative $[\overline{S}(\vec{x}_i) - S_n(\vec{x}_i)]$ deviations from the mean $\overline{S}(\vec{x}_i)$. Also shown in Figure 6a in gray is the

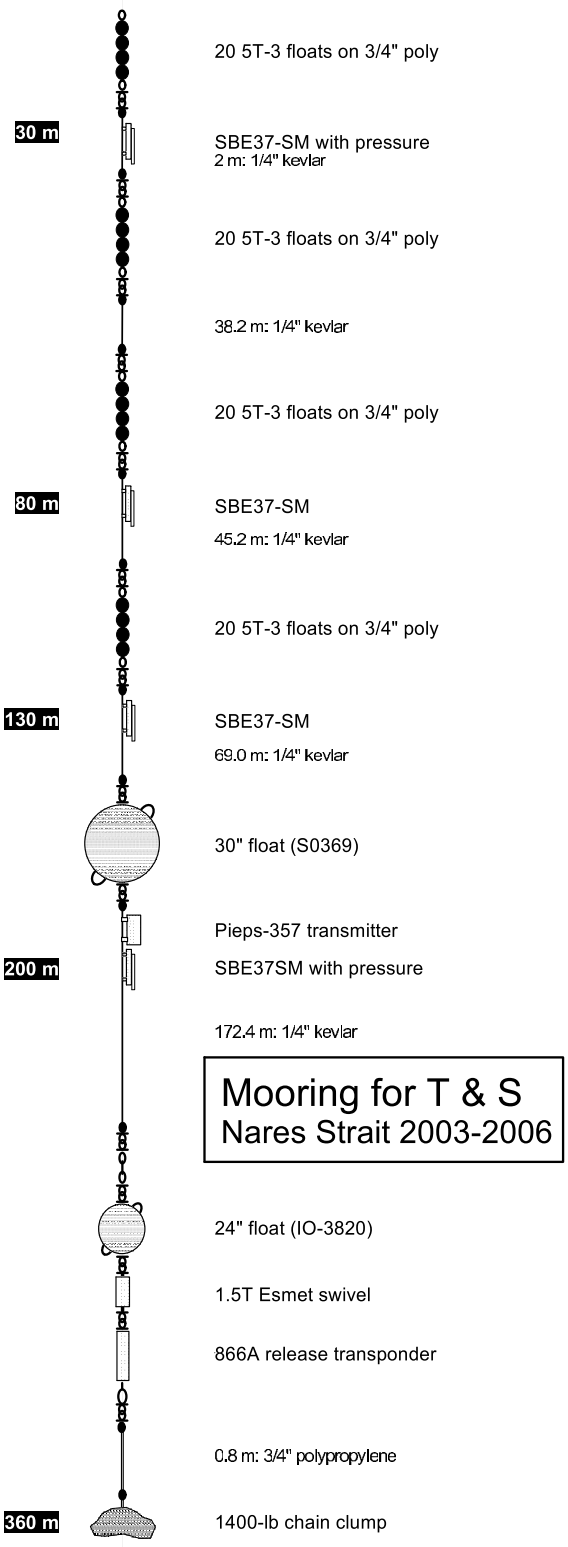

Figure 2. Sketch of CT mooring design. Anchor at the bottom; acoustic release and most of the buoyancy below 200 m; four CT instruments per string at nominal 30, 80, 130, and 200 m with flexible Kevlar cable between instruments. This novel mooring design with low buoyancy in the upper water column allows the mooring to bend under the influence of ice, and profile through the water column at tidal frequencies.

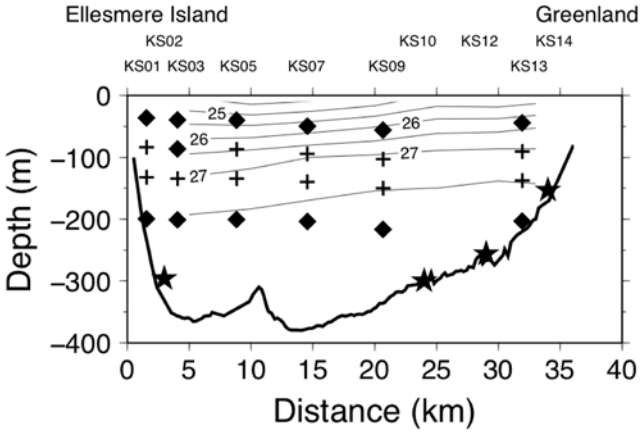

Figure 3. Position of recovered CT moorings and ADCPs in the strait, with Ellesmere Island on the left (west) and Greenland on the right (east). CT moorings consist of four instruments at nominal 30, 80, 130, and 200 m. Crosses and diamonds denote the record-mean depth for each instrument; diamonds show instruments with pressure sensor, whereas crosses show those without. Bottom-mounted ADCPs are shown as stars. Mooring numbering is in sequence starting on the Ellesmere Island side with CT moorings as odd numbers and ADCPs as even numbers. Contour lines represent density anomaly from CTD measurements in 2007.

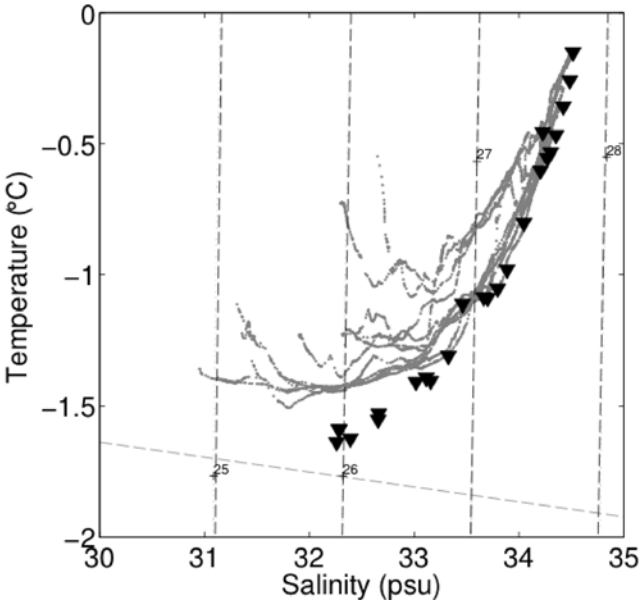

Figure 4. Three-year mean TS diagram from CT mooring data (black triangles) and CTD data across Kennedy Channel during 2007 from the same depth range of 35 to 200 m (gray dots). Also included are the freezing line (light gray dashed) and σ_t lines (dark gray dashed). Note that the westernmost five km of the strait could not be measured by CTD because of heavy ice. All CTD measurements were taken in summer. For salty warm water masses the two different data sets compare well; for fresh cold water masses they diverge.

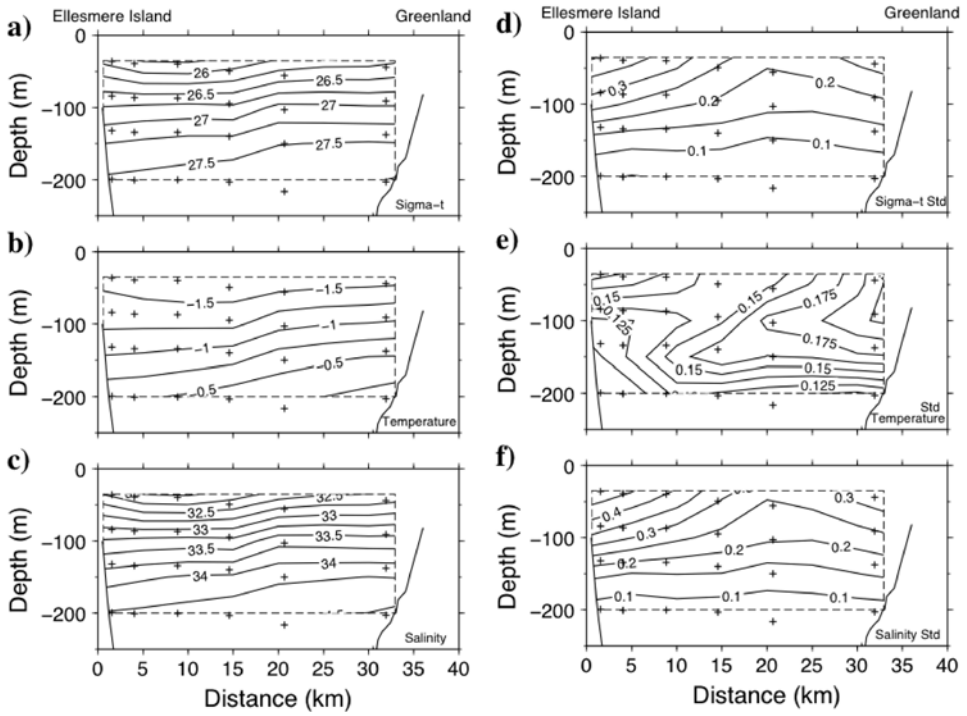

Figure 5. Three-year mean of (a) density anomaly σ_t, (b) temperature, and (c) salinity across the mooring section and standard deviations for (d) density anomaly σ_t, (e) temperature, and (f) salinity. Black crosses denote the instrument record-mean positions. Cold fresh water masses exist on the Ellesmere Island side, getting warmer and saltier with depth and toward Greenland.

ice index following *Münchow and Melling* [2008] to distinguish drift ice from fast-ice conditions. The intervals with a negative index correspond to mobile ice in late summer, autumn, and early winter and those with a positive index correspond to fast-ice conditions in late winter, spring, and early summer. During fast-ice conditions, there is a no-slip constraint on flow at the surface (retarding surface stress). In Figure 6b the gray line represents an annual cycle with minima at the end of August and maxima at the beginning of January.

[23] Mode one (Figure 7a) shows the highest salinity variability in the top 150 m within 20 km of Ellesmere Island with anomalies of up to 0.4 psu from the mean. Strongest gradients occur in the middle of the strait. A zero-line lies along the bottom of the observed section. A second zero line reaches the surface at approximately 10 km from the Greenland coast, so that the top layers on the Greenland side show negative values. This means that change occurs in the same direction across the strait except in the top layers on the eastern side.

[24] The mean plus mode one $[\overline{S}(\vec{x_i}) + S_1(\vec{x_i})]$ (Figure 7b) shows a fresh top layer with salinities of about 32.5 psu across the whole strait. Isohalines shoal slightly upward to the east within 10 km of Ellesmere Island, suggesting an increased geostrophic flow. The positive values in the time series (Figure 6a) coincide with fast-ice conditions, shown by the positive ice index. Variability of short period is much reduced during this time because fluctuations in wind stress cannot influence the strength and direction of current when ice is fast.

[25] The mean minus mode one $[\overline{S}(\vec{x_i}) - S_1(\vec{x_i})]$ (Figure 7c) reveals the freshest water with 31.8 psu in the top layer on the Ellesmere Island side. The 32.5 psu isohaline reaches down to 80 m on the Ellesmere Island side and shoals toward Greenland to about 35 m. Isohalines shoal toward the Greenland side with strongest gradients between 15 and 20 km off Ellesmere Island. The stronger gradient there suggests an increased southward geostrophic flow in the middle of the strait. In the time series (Figure 6a) the negative values coincide with drift ice conditions, as demonstrated by the negative ice index. Such conditions are typically characterized by mobile pack ice on the western side of the strait, with lower ice concentrations or open water to the east. Variability is high during this time because fluctuations in wind stress directly influence the strength and direction of current. This means that during the ice drifting season the implied geostrophic flow is strongest in the top layers in the middle of the strait.

[26] Mode two (Figure 8a) describes a negative region of up to −0.1 psu between 80 and 150 m on the Ellesmere Island side and a positive region with up to 0.3 psu on the Greenland side in a thin top layer. Lateral gradients in the top 80 m are concentrated within 15 km of the Greenland shore. The deepest layer has the same value across the whole strait, close to zero, meaning there is less variability below about 180 m. The opposing signs suggest a seesaw behavior between the top layer and the 80 to 150 m layer closest to Ellesmere Island: if the top layer is saltier than usual, the middle layer on the Ellesmere Island side will be fresher and vice versa.

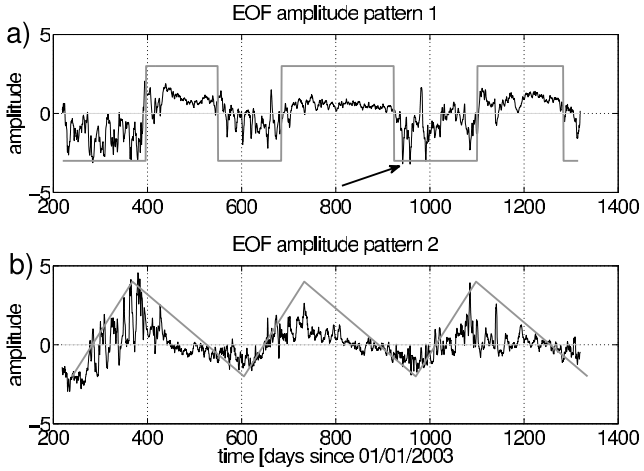

Figure 6. Temporal evolution of eigenfunctions of salinity variability of (a) mode one (54% of the variance) (the arrow marks the strong event in salinity, more than 3 standard deviations from the mean, described in the freshwater incursion section), (b) mode two (19% of the variance). The time series are nondimensional and have a variance of 1. The dark gray line in Figure 6a represents the ice index which is positive for land-fast ice (mid-October–mid-June) and negative for drift ice (mid-June to mid-October) conditions. The dark gray line in Figure 6b represents an idealized annual cycle. The light gray line is the zero line to better distinguish between positive and negative values. The mode one salinity structure appears linked to the state of the ice cover while the mode two structure relates best to the time of year.

[27] The mean plus mode two $[\overline{S}(\vec{x_i}) + S_2(\vec{x_i})]$ (Figure 8b) shows a pattern with reduced stratification and isohalines shoaling toward the Greenland side. Freshest water of about 32.4 psu occurs again on the Ellesmere Island side in the top layers and saltiest water in the lowest layers on the Greenland side with almost 34.5 psu. In the time series (Figure 6b) the positive values in mode two occur between the end of October/beginning of November and mid-March.

[28] The mean minus mode two salinity pattern $[\overline{S}(\vec{x_i}) - S_2(\vec{x_i})]$ (Figure 8c) shows a fresh surface layer with salinities of about 32 psu and isohalines sloping upward to the east in the western half of the strait at depth. The stratification is considerably stronger between about 50 and 150 m. These times characterized by a negative mode two salinity amplitude occur between mid-March and the end of October/beginning of November.

[29] The amplitude of salinity EOF mode one (Figure 6a) clearly changes between fast and drift ice conditions. The amplitude of mode two (Figure 6b) changes on an annual cycle with minima, maxima, and changes in sign occurring at the same time each year. This means mode two is more highly correlated with date than with ice conditions. Since it reflects largely surface changes, we can speculate that it is associated with changes in the amount of surface Arctic meltwater advected through the strait or remotely forced sea-surface height gradients. Based on the analysis above we propose that mode one represents lateral variation across the strait during drift ice conditions and mode two represents a tendency for surface-intensified northward flow, strongest on the Greenland side, to accompany strong southward flow near 100 m depth on the Ellesmere side and vice versa. The modal analysis suggests that ice conditions influence the salinity structure within Nares Strait.

[30] The arrow in Figure 6a denotes a mode one event more than 3 standard deviations from the mean, corresponding to a drop of around 1.6 psu in salinity within 2 days. We describe this large freshwater incursion next.

6. Freshwater Incursion

[31] The data reveal large temporal variability in salinity, especially during drift ice conditions and especially in the upper ocean on the Ellesmere side. One extreme event occurred around year day 942, at the end of July 2005 (also seen in Figure 6a). We here present salinity sections for 2-day means starting at days 938–940 (26–28 July 2005) and continuing throughout the event until days 946–948

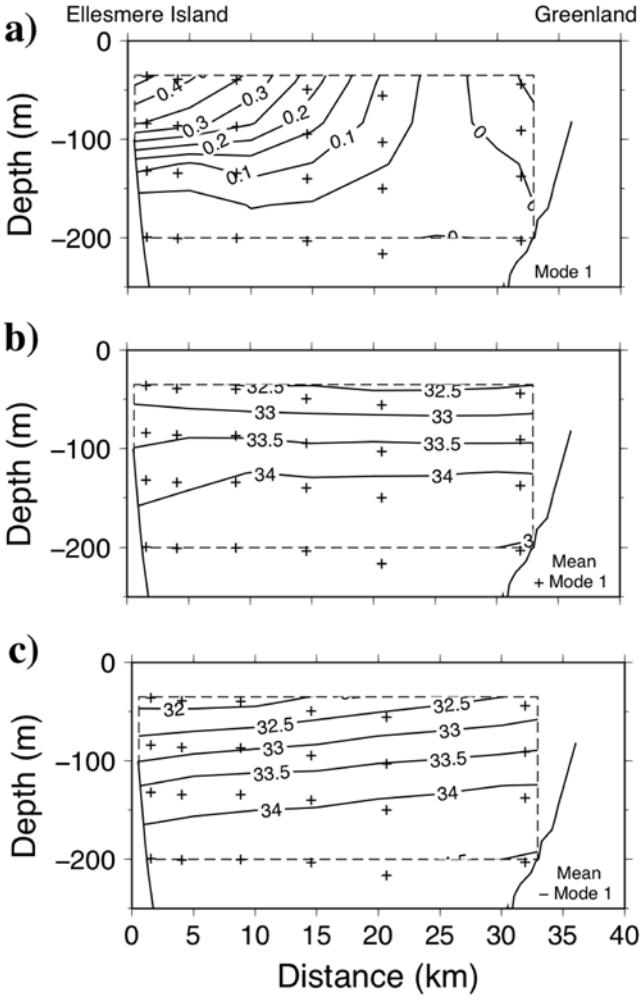

Figure 7. EOF spatial structure of salinity variations shown in combination with the mean salinity field: (a) mode one (54% of the variance), (b) mean plus mode one, (c) mean minus mode one. The contour lines are the same for (b) and (c) for ease of comparison. Black crosses denote the instrument record-mean positions. Mode one explains horizontal variations in salinity especially on the Ellesmere Island side.

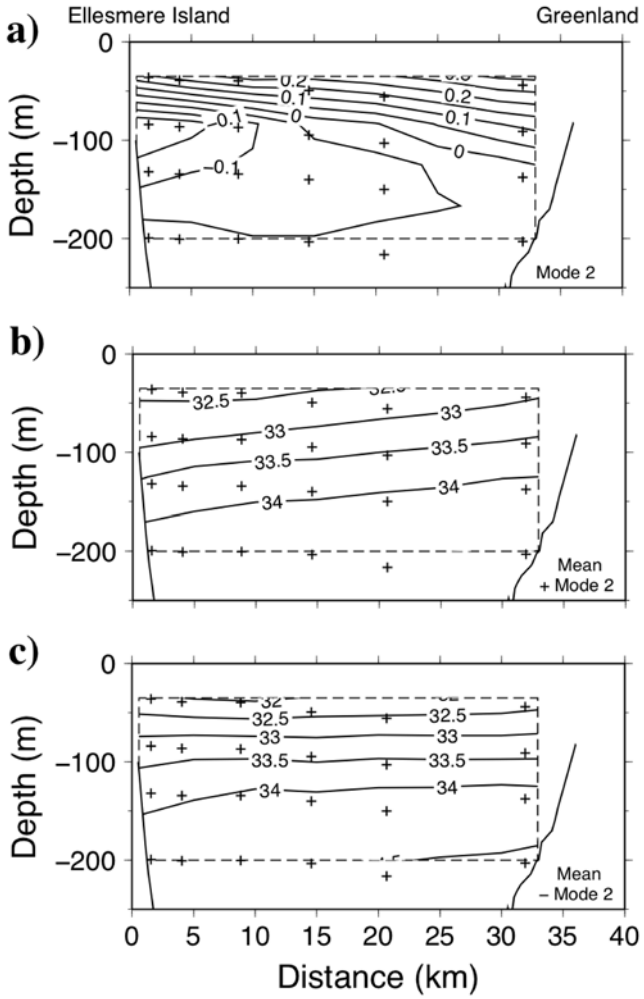

Figure 8. EOF spatial structure of salinity variations shown in combination with the mean salinity field: (a) mode two (19% of the variance), (b) mean plus mode two, (c) mean minus mode two. The contour lines are the same for (b) and (c) for ease of comparison. Black crosses denote the instrument record-mean positions. Mode two shows a tendency for surface-intensified northward flow, strongest on the Greenland side, to accompany strong southward flow near 100 m depth on the Ellesmere side and vice versa.

(3–5 August 2005) (Figure 9). Prior to the event (Figure 9a) we find salinities of around 32 psu in the top layer on the Ellesmere Island side, saltier water at depth and further offshore, and small isohaline slopes. During days 942–944 (Figure 9c) a strong freshwater incursion occurs in the top layer within 15 km of Ellesmere Island. The salinity drops to almost 30 psu (also see Figure 10) and the isohalines move from almost parallel to the sea surface before the event to a steeper slope during this event, especially in the middle of the strait. The 34 psu isohaline, for example, slopes from almost 200 m off Ellesmere Island up to roughly 150 m off Greenland. Using thermal wind, the implied geostrophic velocity for this event, shown in Figure 11, indicates a southward flow in the top layers in the middle of the strait of up to 0.30 m s^{-1}; a reference level velocity of 0.02 m s^{-1} from

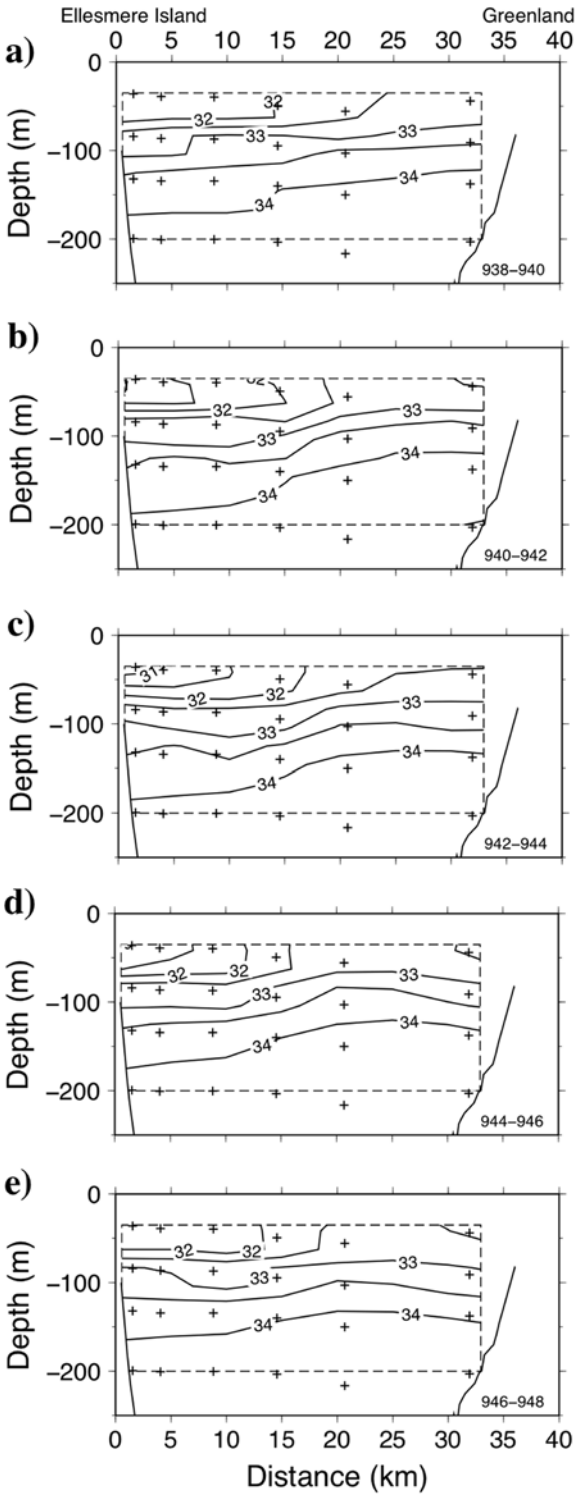

Figure 9. Sections of 2-day mean salinity at year days: (a) 938–940 (26–28 July 2005), (b) 940–942 (28–30 July 2005), (c) 942–944 (30 July–1 August 2005), (d) 944–946 (1–3 August 2005, (e) 946–948 (3–5 August 2005), showing the freshwater incursion in the top layers on the Ellesmere Island side and the sloping of the isohalines, especially in Figure 9c. The contour interval is 0.5 psu in all panels. Black crosses denote the instrument record-mean positions.

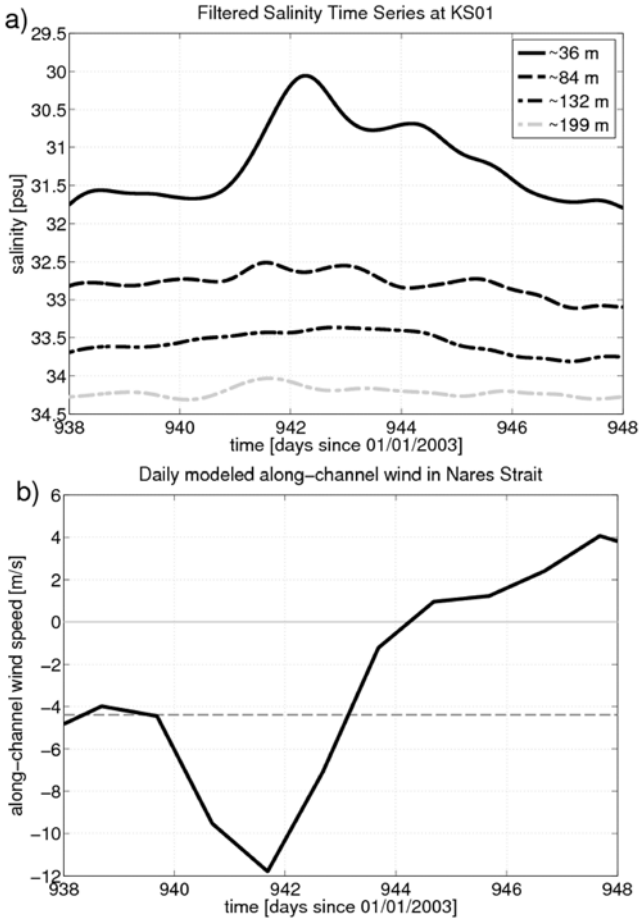

Figure 10. (a) Filtered salinity time series for a 10-day period for all four instruments on the Ellesmere Island side. The strong salinity event during year day 940–942 (28–30 July 2005) shows a surface salinity (record-mean depth of 36 m) on the Ellesmere Island side reduced by almost 2 psu. The black line represent the top instrument on the Ellesmere Island side, the dashed line the second instrument from the top at a record-mean depth of 84 m, the dot-dashed line the third instrument from the top at a record-mean depth of 132 m and the gray dashed line represents the lowest instrument at a record-mean depth of 199 m on the Ellesmere Island side. (b) Daily modeled along-channel wind in Nares Strait for the same 10-day period (black) with negative values representing wind speeds to the south. The dotted dark gray line shows the 3-year mean wind speed. The light gray line is zero wind speed to emphasize a switch in wind direction. A strong southward wind exists between 940–942 (28–30 July 2005) during the same time as the salinity dropped.

ADCP data at 200 m depth during this event was used. Geostrophic velocities of up to 0.20 m s^{-1} exist in the middle of the strait down to about 80 m. Stronger flow also exists in the top layers on the Ellesmere Island side but is less pronounced (0.17 m s^{-1}). At days 944–946 (Figure 9d) this low salinity signal occurs only within 10 km of Ellesmere Island and at days 946–948 (Figure 9e) the signal is present only in a very shallow top layer. Isohalines move back to the original position after the intrusion has passed.

[32] Figure 10a shows the filtered salinity time series for a 2-week period for all instruments on the mooring closest to Ellesmere Island (KS01, instrument mean depths indicated). The top instrument here shows the sharpest drop in salinity of the whole 3-year and 24-instrument record. The other top instruments across the strait exhibit similar but less prominent salinity variations (not shown). The strong signal around day 942 in the top instrument represents a drop from 31.7 psu to 30.1 psu (ΔS). The drop occurs in fewer than 2 days (Δt) and gives a $\frac{\Delta S}{\Delta t} = 0.82$ psu d^{-1}. With depth the signal diminishes, and there is no evidence of the freshening in the lower two instruments. Therefore, the signal is most pronounced close to Ellesmere Island and in the surface layer. If this is a purely advective feature, e.g.,

$$\frac{\partial S}{\partial t} \sim u \frac{\partial S}{\partial x}, \tag{2}$$

then we can calculate Δx, the along-channel length scale. With $u \sim 0.30$ m s^{-1} and $\Delta S^x \sim 1.6$ psu we find $\Delta x \sim 50$ km. This is the distance that a water parcel would get advected during this strong event if the salinity anomaly observed was a purely advective feature. Downwelling favorable winds from the north and associated southward advection of ice along Ellesmere Island contributed to this extreme event. Figure 10b shows the predicted along-channel wind during the freshwater incursion from a mesoscale atmospheric circulation model by *Samelson and Barbour* [2008]; no direct observations exist. Wind speeds reach 12 m s^{-1} to the south on day 942 (30 July 2005), before the wind slows down and eventually changes direction. Satellite images reveal that the western half of the strait was covered by heavy ice at this time (Figure 12). Southward ice drift measured by Doppler sonar at site KS02 ranged between 0.5 and 1.5 m s^{-1} during days 937–943 (25–31 July 2005). Rapid ice drift and the

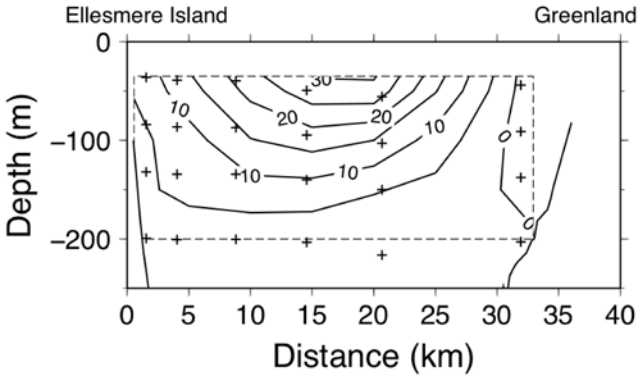

Figure 11. The geostrophic velocity section during the strong salinity event in cm s^{-1}. Black crosses denote the instrument record-mean positions. Positive values denote flow to the south. A reference velocity of 0.02 m s^{-1} from ADCP mooring data during this event is used as a level of known motion at 200 m. The surface-intensified flow is most pronounced in the middle of the strait with values of up to 0.30 m s^{-1}. A stronger flow also exists on the Ellesmere Island side.

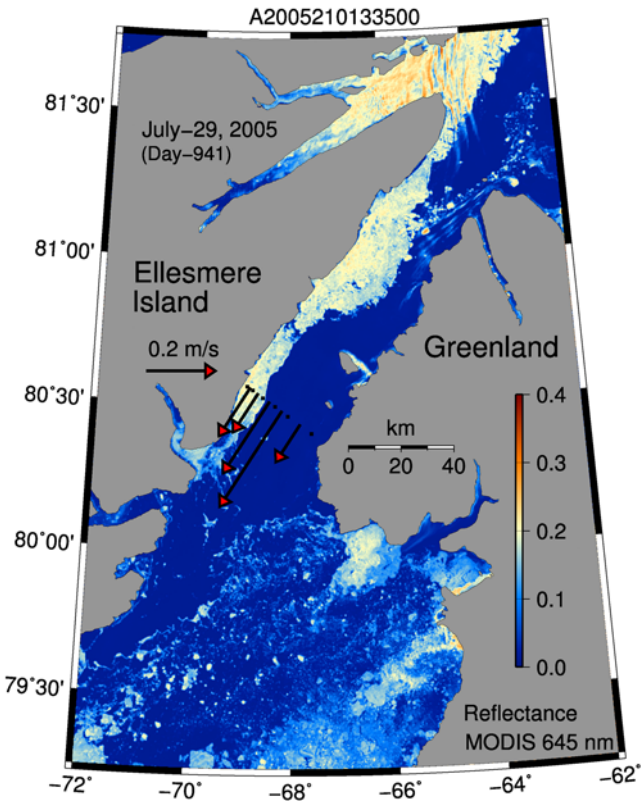

Figure 12. Modis image, 654 nm band, reflectance represents ice (yellow) and water (blue) for 29 July 2005 during strong event. Overlaid are vectors of geostrophic velocity in top layers during the strong event.

wind data confirm that this event was indeed forced by strong wind from the north.

7. Discussion

[33] Using thermal wind, we calculate the 3-year mean geostrophic velocity for depths between 35 and 200 m, estimated from measured hydrographic properties that are averaged over the observational period (Figure 4) with a level of known motion from ADCP data. This calculation captures the baroclinic component of the geostrophic flow from the CT data plus the component introduced by the reference ADCP velocity and is shown in Figure 13. Positive velocities indicate a flow to the south. Shear in geostrophic velocity occurs mainly in the upper 150 m. The section shows a surface-intensified southward flow on the Ellesmere Island side of up to 0.20 m s^{-1} and high mean velocities of up to 0.14 m s^{-1} in the middle of the strait.

[34] *Münchow and Melling* [2008] show a time-mean and depth-averaged northward flowing current of 0.04 ± 0.01 m s^{-1} close to Greenland from the 3-year ADCP data set that is not apparent in the geostrophic flow field (Figure 13) because the CT section does not reach the Greenland shore. CT measurements closest to the Greenland side show warm and salty water of Atlantic origin at depth. One possible origin of Atlantic water with warm and salty characteristics in Nares Strait is from the south via an extension of the West Greenland Current in the northward flowing current on the Greenland shelf. Most of the West Greenland Current turns cyclonically west across Baffin Bay while following the 500 m isobath but a fraction continues north along the Greenland coast [*Bourke et al.*, 1989; *Melling et al.*, 2001; *Bacle et al.*, 2002]. Another possibility is that Atlantic water is advected from the north through the Arctic Ocean. The Atlantic source water flowing through Nares Strait is coming mainly from the Barents Sea branch lower halocline [*Rudels et al.*, 2004]. Below 100 m depth in Nares Strait up to 80% of the water is traceable to the North Atlantic Ocean [*Jones and Eert*, 2006]; *Münchow et al.* [2007] also found water of Atlantic origin in the deeper layers in Nares Strait. *Jones et al.* [2003] conclude, based on nutrient data, that the most likely origin of Atlantic water in Smith Sound is the Arctic Ocean.

[35] Channel flows in a rotating frame of reference are often controlled by friction and geostrophy [*Gill*, 1982]. Stratified flows scale with the internal Rossby radius of deformation. In Nares Strait this radius is about 10 km [*Münchow et al.*, 2006] and sets the width of baroclinic flow in geostrophic balance [*LeBlond*, 1980; *Gill*, 1982]. With the ~5 km spatial resolution of our moorings in Nares Strait the internal Rossby radius of deformation is resolved and we thus are confident to interpret the spatial structure of the flow. This spatial scale is evident during a particularly strong salinity event when the fresh outflow from the Arctic Ocean is concentrated within 10 km of Ellesmere Island. The spatial structure of anomalies apparent in the EOFs of salinity also indicates that spatial variation is largely confined within an internal deformation radius of the western and eastern shorelines.

8. Conclusions

[36] We have had success with an innovative mooring designed to support CT sensors at shallow depth while minimizing risk from icebergs in Nares Strait. The moorings' small components and low net buoyancy within the domain

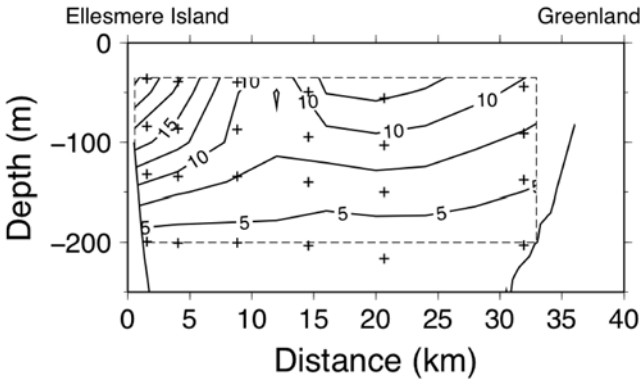

Figure 13. The 3-year mean geostrophic velocity section in cm s^{-1}. Black crosses denote the instrument record-mean positions. Positive values denote flow to the south. A reference velocity of 0.04 m s^{-1} from the lateral and time-mean ADCP data is used as a level of known motion at 200 m. The surface-intensified flows on the Ellesmere Island side and in the middle of the strait are most pronounced with values of up to 0.20 and 0.14 m s^{-1}, respectively.

of greatest risk above a depth of 200 m allow it to be drawn down out of harms way when current (and iceberg drift) is fast.

[37] Nares Strait is "wide" in the sense that its width exceeds the internal deformation radius by a factor of about 4. It is clear that the high spatial resolution of our moored array in Nares Strait is essential to elucidate ocean features in this strait.

[38] A frequency domain linear system analysis was used to minimize the "noise" arising from the drawdown of sensors. While not without limitations, this method improves signal-to-noise ratios and thus statistical confidence from our 3-year observational study of Nares Strait.

[39] The 3-year mean geostrophic current flows southward on the western side of the channel. Direct measurements by ADCP near the coast of Greenland during the same time period [*Münchow and Melling*, 2008] indicate that current flows northward there. As a 3-year average, the geostrophic flow through the section in Kennedy Channel is southward and surface intensified with a maximum of 0.20 m s^{-1} on the Ellesmere Island side and a secondary maximum of 0.14 m s^{-1} at the shallowest depth of measurement (35 m) near the middle of the section, including a reference level velocity from ADCP data (discussed in *Münchow and Melling* [2008]). This long-term average flow structure is qualitatively consistent with synoptic snapshots in summer using vessel-mounted ADCP [*Münchow et al.*, 2006, 2007] and with measured enhanced drawdown of the CT moorings positioned near the center of the strait [*Münchow and Melling*, 2008].

[40] The waters found on opposite sides of Nares Strait have different characteristics. Those on the western (Ellesmere) side are colder and less saline than those on the Greenland side. Isopycnals generally have their maximum slope near the middle of the strait, consistent with the enhanced geostrophic velocity here. The freshest, coldest water is found near the sea surface on the Ellesmere Island side, flowing southward from the Arctic Ocean as a buoyant outflow similar to a coastal current [*Yankovsky et al.*, 2000; *Bacon et al.*, 2002; *Chapman*, 2003; *Pickart et al.*, 2005]. Over the 3-year survey the greatest temporal variability in salinity was observed within this cold outflow. In contrast, the greatest temporal variability in temperature was observed on the Greenland side. Variability is small at depth where waters are isolated from surface salt and heat fluxes by ice cover and by a statically stable water column.

[41] An EOF analysis of salinity variations across the section has revealed two modes that together explain 3/4 of the total variance. Mode one is surface-intensified and has maximum amplitude at the coast of Ellesmere Island; with negative eigenvalue it represents a south-flowing buoyant boundary current. Mode two represents a tendency for surface-intensified northward flow, strongest on the Greenland side, to accompany strong southward flow near 100 m depth on the Ellesmere side and vice versa. Interplay of these modes can create a seesaw behavior between the Ellesmere and Greenland sides of the strait and between the top and the middle depths close to Ellesmere Island. When the top layer is saltier, the midlayer on the Ellesmere Island side is fresher and vice versa, resulting in times of small and large vertical stratification.

[42] The sea ice of Nares Strait alternates between drifting and fast conditions on an irregular annual cycle. Ice is most commonly drifting during late summer, autumn, and early winter and most commonly fast during late winter, spring, and early summer. The ice index switches between the two phases and was defined by *Münchow and Melling* [2008]. The first EOF mode of salinity variations appears to be correlated with the state of the ice cover, so the cross-strait variation in surface salinity is strongest during drifting ice conditions. The annual modulation of the second EOF model of salinity variations appears better correlated with date than with ice condition; the variation is large and positive at the beginning of January (high surface salinity) and large and negative at the end of August (low surface salinity). In combination, these modes create strong geostrophic current near the ocean surface midstrait in late summer and a subsurface jet of geostrophic current adjacent to Ellesmere in midwinter.

[43] The most intense anomaly in salinity occurred in July 2005. Salinity at 35 m depth decreased by close to 2 psu over 2 days and isohalines shoaled sharply near the middle of the strait. This event can also be seen in the principal component time series of the first EOF mode of salinity with a large, negative amplitude indicating a location near the surface on the Ellesmere side. The associated geostrophic flow was southward at 0.30 m s^{-1} in the top layers in the middle of the strait. At the same time, a rapid ice export within the Rossby radius of deformation close to Ellesmere Island existed, associated with strong southward winds.

[44] Clearly anomalies in flow and in salt deficit are correlated during fluctuations with period as short as a few days in Nares Strait. For this reason a quick calculation of freshwater flux by multiplication of the mean field of current times that of salinity deficit will be biased low by an amount not known at this time. Moreover, there are two other sources of appreciable negative bias that we do not yet have a handle on. The first arises from our lack of observations of salinity and current in the upper 35 m of the ocean, where momentum and freshwater are very strongly concentrated. The second arises from our lack of observations within the 20% of the 38 km cross section within one Rossby scale of the coastlines of Greenland and Ellesmere Island. The poorly understood interaction of geostrophic and frictional effects in these lateral boundary layers is a disincentive to casual interpolation of data across them at his time. We therefore postpone a careful presentation of our best knowledge of volume and freshwater fluxes through Nares Strait to a future publication.

Appendix A: Signal Processing

A1. Pressure Interpolation

[45] We have interpolated values of pressure between CT instruments at nominal depths of 30 and 200 m to the locations of the two instruments at intermediate nominal depths of 80 and 130 m assuming a linear variation of pressure along our mooring line (a straight line when the mooring is tipped over). Linear interpolation has been justified via simulations of mooring performance in current by a static mooring model [*Bell*, 1979], which predicts a linear behavior for our mooring design.

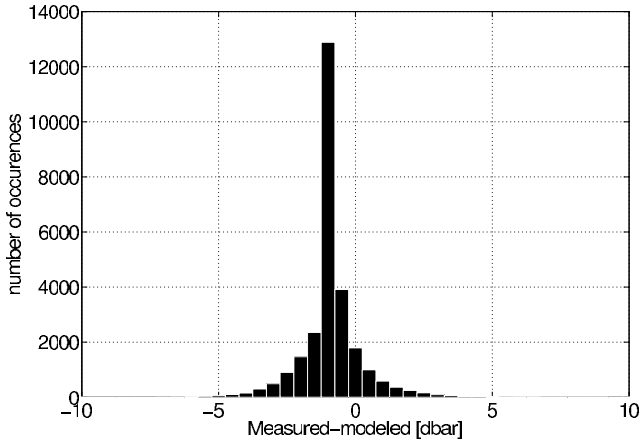

Figure A1. Pressure intercomparison between measured pressure at 80 m at KS03 and modeled pressure assuming linear behavior after mooring model results [*Bell*, 1979]: histogram of measured minus modeled pressure shows a Gaussian distribution, that is, a linear interpolation explains the mooring behavior well.

[46] Testing this assumption, we use the KS03 pressure record at a nominal depth of 80 m (Figure 3) for an intercomparison of the interpolated pressure with actually measured pressure. A linear regression between the modeled pressure p_{mod} and the measured pressure p gives

$$p_{\mathrm{mod}} = 0.9867p + 2.0364 \tag{A1}$$

and explains 99% of the variance. The unexplained variance suggests an interpolation error of about ±3 dbar at 95% confidence. The histogram (Figure A1) reveals that the distribution of modeled minus measured pressure is Gaussian. Therefore the modeled pressure represents the actual pressure of that instrument well. The nonzero intercept for the regression could be caused by the slightly shallower actual mooring depth (instrument two was located at 79 m at zero drawdown) or uncertainties in the model calculations or input velocities. We will exploit accurate pressure estimates at all instruments at all times in the subsequent linear system analysis to minimize the impact of mooring motion. We then calculate salinity from conductivity, in situ temperature, and pressure using the standard algorithm [*UNESCO*, 1983], as well as the density anomaly σ_t.

A2. Linear System Analysis

[47] Mooring motions lead to large variations in pressure and corresponding salinity and temperature variations in the raw time-series data. These variations occur mostly at tidal periods because tidal currents constitute almost 93% of total current variance in Nares Strait [*Münchow and Melling*, 2008]. In order to analyze time-series data from CT sensors we need to minimize the effects of both mooring motion and tides.

[48] Figure A2 shows the raw pressure data for a 50-day segment of the 3-year time series from the instrument near the surface and closest to Ellesmere Island (KS01). It reveals the dominant tidal influence on the instruments depth as the drawdown varies from 0 to 50 m. Vertical motion of instruments is smaller lower down on the mooring; for example, it is only about 10 m at 200 m depth (not shown).

[49] To reduce this signal caused by mooring motion we use the pressure data to remove the part of the salinity (temperature) signal that is coherent with the drawdown through a frequency domain linear system analysis. *Münchow et al.* [1992] and *Münchow* [1998] have previously used this method to reduce noise due to sea level changes (local winds and freshwater discharge) in current data. We assume a single input/single output linear system. The single input/single output model looks like the following:

$$p(t) \rightarrow \boxed{\mathrm{H(f)}} \rightarrow y(t) = y_c(t) + y_{ic}(t), \tag{A2}$$

where $p(t)$ is pressure (measured input), $H(f)$ is the linear transfer function as a function of frequency f [the frequency response function of a constant-parameter linear system between $p(t)$ and $y(t)$] with $y(t)$ as the salinity and temperature measurements (measured output), $y_c(t)$ is the component that is coherent (subscript c) with pressure fluctuations, and $y_{ic}(t)$ is the component that is incoherent (subscript ic) with pressure fluctuations. We assume that the salinity and temperature signals consist of two components (coherent plus incoherent).

[50] In order to find the signal $y_{ic}(t)$, we estimate H as a function of frequency f between $p(t)$ and $y(t)$ as

$$Y(f) = H(f)P(f) + Y_{ic}(f), \tag{A3}$$

where $Y(f)$ and $P(f)$ are the Fourier transforms of $y(t)$ and $p(t)$, respectively, while $Y_{ic}(f)$ is the signal that is incoherent with the pressure fluctuations. We find the time series of interest for subsequent analyses $y_{ic}(t)$ from the inverse Fourier transform, that is,

$$y_{ic}(t) = F^{-1}[Y(f) - H(f)P(f)]. \tag{A4}$$

[51] The method is applied separately to data from individual instruments, using a time series of pressure (i.e., depth) and either salinity or temperature. Since it is an analysis of variations the average value of each time series is subtracted before the method is applied and will be added back in to the incoherent part of the variability to give the final time series.

[52] Figure A2b shows the raw salinity data (before the mean is removed) that includes both coherent and incoherent parts with pressure. Figures A2c and A2d show the coherent and incoherent parts of the salinity signal, respectively, with the mean added back in, for the sample 50-day time series. The resultant time series are assumed to represent a variable at the record-mean depth for each instrument where their locations are shown as symbols in Figure 3.

[53] The linear system analysis relies on several assumptions. First, it assumes that a change in the depth of the instrument via drawdown in the tidal flow generates a proportional change in salinity (or temperature). However, the change in salinity (or temperature) with drawdown is equally influenced by the vertical derivative in that characteristic, which is not part of the linear system. In the extreme case where the vertical derivative approaches zero, salinity (or temperature) does not change in response to drawdown; this is visible, for example, during days 275–313 in Figure A2.

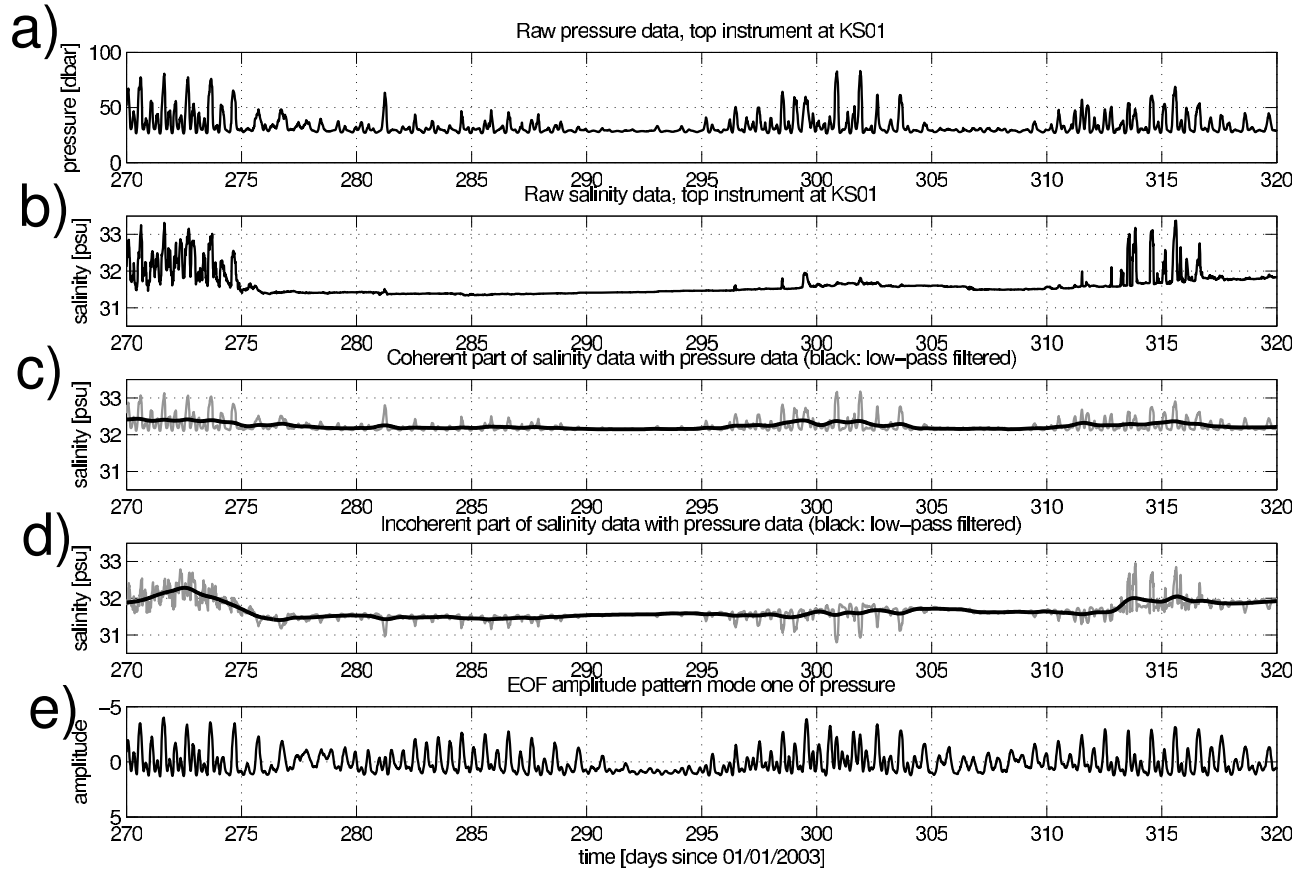

Figure A2. Evolution from raw pressure and salinity data to low-pass-filtered pressure-incoherent salinity data that will be used for further analysis, as well as mode one amplitude of the pressure EOF analysis. All plots are shown for a sample 50-day time series: (a) raw pressure data at top instrument at KS01 on Ellesmere Island side showing tidal variations; (b) raw salinity data at top instrument at KS01 on Ellesmere Island side, including the mean; (c) part of the salinity that is coherent with pressure in gray; (d) part of the salinity that is incoherent with pressure in gray; and (e) amplitude of the first mode of the pressure EOF analysis, explaining 71% of the variance in the 3-year pressure time series (the time series is nondimensional and has a total variance of 1). The black lines in Figures A2 and A2 show the low-pass-filtered salinity signal. The low-pass-filtered incoherent part of the salinity (and temperature) will be used in the subsequent analysis.

[54] Second, the linear system analysis treats the time series as statistically stationary and ergodic; that is, it assumes that the data have statistical properties that are invariant with translations in time [*Bendat and Piersol*, 1993]. As a consequence the linear transfer function $H(f)$ represents an average over intervals wherein fluctuations are large (days 270–275) and intervals wherein they are small (days 275–313). Since we use $H(f)$ to deconvolve drawdown effects from the whole time series, the corrections are insufficient during certain intervals (like days 270–275) and introduce spurious "incoherent" signal during other intervals (e.g., days 275–313). With salinity, for which drawdown always increases the value, the "incoherent" value is too high where the deconvolution falls short and too low where the deconvolution is too enthusiastic. These imperfections of the linear systems analysis have, as we demonstrate, little impact on the discussion of subtidal variability because most of the mooring motion is caused by tidal currents. Hence we interpret the linear system analysis as a preprocessing step that increases signal-to-noise ratios by reducing substantial noise prior to the application of low-pass filters.

A3. Filters

[55] Removing signals with frequencies higher than tidal, we filter the pressure-coherent $y_c(t)$ and pressure-incoherent $y_{ic}(t)$ parts of each salinity and temperature time series with a Lanczos raised-cosine low-pass filter that has a cut-off period near 40 h and a window width of 50 h. Figures A2c and A2d show the low-pass-filtered time series of pressure-coherent and pressure-incoherent salinity, respectively, for the example 50-day window, in black. The incoherent part $y_{ic}(t)$ has a similar signature as the raw salinity signal. Note that some tidal signals are still present in the incoherent part $y_{ic}(t)$ prior to filtering. These may arise from either tidal advection of horizontal property gradients or imperfections of the linear systems analysis. Low-pass filtering removes

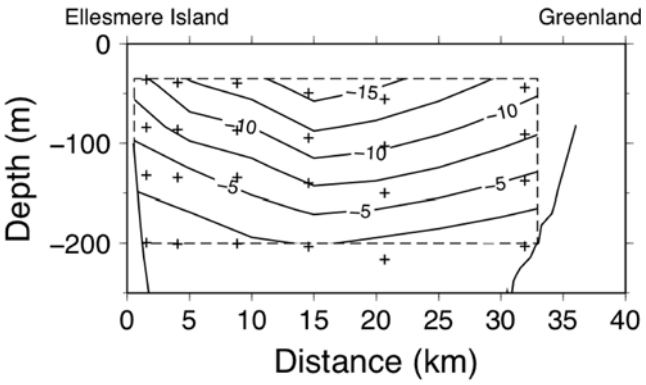

Figure B1. Spatial pattern of pressure EOF analysis, mode one, explaining 72% of the variance, in dbar, scaled by the factor that was used to achieve a variance of 1 in the time series. Black crosses denote the instrument record-mean positions. Highest variability of up to 17 dbar is observed at instruments in the top layers in the middle of the strait. Mooring motions are strongly correlated at all locations.

these tidal signals. Our analyses will use these low-pass-filtered data that are incoherent with pressure fluctuations.

Appendix B: Empirical Orthogonal Functions

[56] EOFs were first introduced to atmospheric science by *Lorenz* [1956] and later to oceanography by *Davis* [1976] and *Kundu and Allen* [1976]. We here apply them to the pressure data to demonstrate that our entire sensor array moves in a largely correlated fashion in response to tidal currents. Furthermore, in section 5 we discuss spatial and temporal salinity variations as seen in the EOFs.

[57] EOFs decompose observations $S(\vec{x_i}, t_k)$ at $\vec{x_i} = (x, z)_i$ with $i = 1, 2, \ldots I = 24$ discrete locations in the strait and t_k with $k = 1, 2, \ldots K = 105654$ samples in time into mutually uncorrelated (orthogonal) modes of variability. Each mode has a temporal amplitude $a_n(t_k)$ and a spatial pattern $\phi_n(\vec{x_i})$ for the $n = 1, 2, \ldots N = 24$ modes, that is

$$S(\vec{x_i}, t_k) = \sum_{n=1}^{N} [a_n(t_k) * \phi_n(\vec{x_i})]. \quad \text{(B1)}$$

$a_n(t_k)$ are eigenfunctions and $\phi_n(\vec{x_i})$ are eigenvectors to an eigenvalue problem

$$R_{i,n} * \phi_n(\vec{x_i}) = \lambda_n * \phi_n(\vec{x_i}) \quad \text{(B2)}$$

with $R_{i,n}$ being the zero-lag cross-covariance matrix of size 24*24 of the observations at locations $(\vec{x_i})$. λ_n is the eigenvalue for the n-th mode and is interpreted as the variance associated with the n-th mode. The functions $a_n(t_k)$ and $\phi_n(\vec{x_i})$ are subject to an orthogonality condition

$$\sum_{i=1}^{I} \phi_n(\vec{x_i}) * \phi_m(\vec{x_i}) = \delta_{nm} \quad \text{(B3)}$$

with δ_{nm} being the Kronecker delta with $\delta = 0$ for $n \neq m$ and $\delta = 1$ for $n = m$.

[58] We performed an EOF analysis on the raw pressure data; a 50-day sample period is shown in Figure A2a. Figure A2e shows the temporal evolution of the first mode $a_1(t_k)$ that represents 71% of the variance. The time series is nondimensional and has a zero mean and a normalized variance of 1. Figure B1 depicts the corresponding spatial pattern of mode one, that is, $\phi_1(\vec{x_i})$ in dbar. This fixed pattern in space is modulated in time by values shown in Figure A2e. In the spatial pattern we find the same sign across the strait with highest variability of about 17 dbar in the surface layer in the middle of the strait and values close to zero at around 200 m. The maximum vertical excursion in the deeper center of the channel is expected, as both tidal and subtidal currents are largest near this location [*Münchow and Melling*, 2008]. Our results indicate that the mooring motion is strongly correlated at all instrument locations (Figures A2e and B1).

[59] **Acknowledgments.** We thank the officers and crew of USCGC *Healy* and CCGS *Henry Larsen* for all their hard work during deployment and recovery. We also thank the capable technicians (Peter Gamble, Jo Poole, Ron Lindsay, and Dave Huntley), who were essential to the success of the mooring component of this project. We also thank the two anonymous reviewers for their suggestions. Support for this work comes from the National Science Foundation from grant 0230236 and we acknowledge financial and in-kind support from Fisheries and Oceans Canada and from the Canadian Federal Programme for the International Polar Year Programme's for the Canadian Arctic Throughflow study (IPY 2006-SR1-CC-135). H.L.J. is funded by a Royal Society University Research Fellowship, for which she is very grateful.

References

Aagaard, K., and E. C. Carmack (1989), The role of sea ice and other fresh water in the Arctic circulation, *J. Geophys. Res.*, *94*(C10), 14,485–14,498.

Bacle, J., E. Carmack, and R. Ingram (2002), Water column structure and circulation under the North Water during spring transition: April–July 1998, *Deep-Sea Res., Part II*, *49*(22–23), 4907–4925.

Bacon, S., G. Reverdin, I. Rigor, and H. Snaith (2002), A freshwater jet on the East Greenland Shelf, *J. Geophys. Res.*, *107*(C7), 3068, doi:10.1029/2001JC000935.

Bell, W. (1979), A three-dimensional subsurface mooring model. Pacific Marine Science Report 79-20, Fisheries and Oceans Canada, Institute of Ocean Sciences, Sidney, Canada.

Bendat, J., and A. Piersol (1993), *Engineering Applications of Correlations and Spectral Analysis*, 458 pp., John Wiley & Sons, New York, N.Y.

Bourke, R., V. Addison, and R. Paquette (1989), Oceanography of Nares Strait and northern Baffin Bay in 1986 with emphasis on deep and bottom water formation, *J. Geophys. Res.*, *94*(C6), 8289–8302.

Chapman, D. (2003), Separation of an advectively trapped buoyancy current at a bathymetric bend, *J. Phys. Oceanogr.*, *33*(5), 1108–1121.

Coachman, L. K., and K. Aagaard (1966), On water exchange through Bering Strait, *Limnol. Oceanogr.*, *11*(1), 44–59.

Davis, R. (1976), Predictibility of sea surface temperature and sea level pressure anomalies over the North Pacific Ocean, *J. Phys. Oceanogr.*, *6*, 249–266.

Dickson, R. R., J. Meincke, S. A. Malmberg, and A. J. Lee (1988), The Great Salinity Anomaly in the northern North-Atlantic 1968–1982, *Progr. Oceanogr.*, *20*(2), 103–151.

Fahrbach, E., J. Meincke, S. Østerhus, G. Rohardt, U. Schauer, V. Tverberg, and J. Verduin (2001), Direct measurements of volume transports through Fram Strait, *Polar Res.*, *20*(2), 217–224.

Gill, A. E. (1982), *Atmosphere-Ocean Dynamics*, 662 pp., Academic Press, Orlando, Fla.

Goosse, H., T. Fichefet, and J. M. Campin (1997), The effects of the water flow through the Canadian Archipelago in a global ice-ocean model, *Geophys. Res. Let.*, *24*(12), 1507–1510.

Harms, S., and C. Winant (1998), Characteristic patterns of the circulation in the Santa Barbara Channel, *J. Geophys. Res.*, *103*(C2), 3041–3065.

Jones, E., and A. Eert (2006), Water of Nares Strait in 2001, *Polarforschung*, *74*(1–3), 186–189.

Jones, E., J. Swift, L. Anderson, M. Lipizer, G. Civitarese, K. Falkner, G. Kattner, and F. McLaughlin (2003), Tracing Pacific water in the North

Atlantic Ocean, *J. Geophys. Res.*, *108*(C4), 3116, doi:10.1029/2001JC001141.
Koenigk, T., U. Mikolajewicz, H. Haak, and J. Jungclaus (2007), Arctic freshwater export in the 20th and 21st centuries, *J. Geophys. Res.*, *112*(G4), G04S41, doi:10.1029/2006JG000274.
Kundu, P., and J. Allen (1976), Some three-dimensional characteristics of low-frequency current fluctuations near the Oregon coast, *J. Phys. Oceanogr.*, *6*, 181–199.
LeBlond, P. H. (1980), On the surface circulation in some channels of the Canadian Arctic Archipelago, *Arctic*, *33*(1), 189–197.
Lorenz, E. (1956), Empirical orthogonal functions and statistical weather predictions, in *Scientific Report No. 1*, Statistical Forecasting Project, Dept. of Meteorology, MIT, Cambridge, Mass.
Melling, H., Y. Gratton, and G. Ingram (2001), Ocean circulation within the North Water polynya of Baffin Bay, *Atmos. Ocean*, *39*(3), 301–325.
Melling, H., et al. (2008), Fresh-water fluxes via Pacific and Arctic outflows across the Canadian polar shelf, in *Arctic-Subarctic Ocean Fluxes*, edited by R. R. Dickson, J. Meincke, and P. Rhines, pp. 193–261, Springer, Berlin.
Münchow, A. (1998), Tidal currents in a topographically complex channel, *Cont. Shelf Res.*, *18*(5), 561–584.
Münchow, A., and R. Chant (2000), Kinematics of inner shelf motions during the summer stratified season off New Jersey, *J. Phys. Oceanogr.*, *30*(2), 247–268.
Münchow, A., and H. Melling (2008), Ocean current observations from Nares Strait to the west of Greenland: Interannual to tidal variability and forcing, *J. Mar. Res.*, *66*(6), 801–833.
Münchow, A., A. Masse, and R. Garvine (1992), Astronomical and nonlinear tidal currents in a coupled estuary shelf system, *Cont. Shelf Res.*, *12*(4), 471–498.
Münchow, A., K. Falkner, and H. Melling (2007), Spatial continuity of measured seawater and tracer fluxes through Nares Strait, a dynamically wide channel bordering the Canadian Archipelago, *J. Mar. Res.*, *65*(6), 759–788.
Münchow, A., H. Melling, and K. K. Falkner (2006), An observational estimate of volume and freshwater flux leaving the Arctic Ocean through Nares Strait, *J. Phys. Oceanogr.*, *36*(11), 2025–2041.
Padman, L., and S. Erofeeva (2004), A barotropic inverse tidal model for the Arctic Ocean, *Geophys. Res. Lett.*, *31*, L02303, doi:10.1029/2003GL019003.
Pickart, R. (2004), Shelfbreak circulation in the Alaskan Beaufort Sea: Mean structure and variability, *J. Geophys. Res.*, *109*, C04024, doi:10.1029/2003JC001912.
Pickart, R., D. Torres, and P. Fratantoni (2005), The East Greenland Spill Jet, *J. Phys. Oceanogr.*, *35*(6), 1037–1053.
Prinsenberg, S. J., and E. B. Bennett (1989), Vertical variations of tidal currents in shallow land fast ice-covered regions, *J. Phys. Oceanogr.*, *19*(9), 1268–1278.
Prinsenberg, S. J., and J. Hamilton (2005), Monitoring the volume, freshwater and heat fluxes passing through Lancaster Sound in the Canadian Arctic Archipelago, *Atmos. Ocean*, *43*(1), 1–22.
Rudels, B., E. Jones, U. Schauer, and P. Eriksson (2004), Atlantic sources of the Arctic Ocean surface and halocline waters, *Polar Res.*, *23*(2), 181–208.
Sadler, H. (1976), Water, heat, and salt transport through Nares Strait, Ellesmere Island, *J. Fish. Res. Board Can.*, *33*, 2286–2295.
Samelson, R., and P. Barbour (2008), Low-level winds in Nares Strait: A model-based mesoscale climatology, *Mon. Weather Rev.*, *136*, 4746–4759.
Schauer, U., H. Loeng, B. Rudels, V. K. Ozhigin, and W. Dieck (2002), Atlantic Water flow through the Barents and Kara Seas, *Deep-Sea Res.*, *49*(12), 2281–2298.
Schauer, U., E. Fahrbach, S. Østerhus, and G. Rohardt (2004), Arctic warming through the Fram Strait: Oceanic heat transport from 3 years of measurements, *J. Geophys. Res.*, *109*, C06026, doi:10.1029/2003JC001823.
Steele, M., D. Thomas, D. Rothrock, and S. Martin (1996), A simple model study of the Arctic Ocean freshwater balance, 1979–1985, *J. Geophys. Res.*, *101*(C9), 20,833–20,848.
Sutherland, D. A., and R. S. Pickart (2008), The East Greenland Coastal Current: Structure, variability, and forcing, *Progr. Oceanogr.*, *78*(1), 58–77.
Tang, C. L., Q. Gui, and B. M. DeTracey (1999), A modeling study of upper ocean winter processes in the Labrador Sea, *J. Geophys. Res.*, *104*(C10), 23,411–23, 425.
UNESCO (1983), Algorithms for computation of fundamental properties of seawater, *UNESCO Tech. Pap. Mar. Sci.*, *44*, 58.
Wadley, M. R., and G. R. Bigg (2002), Impact of flow through the Canadian Archipelago and Bering Strait on the North Atlantic and Arctic circulation: An ocean modelling study, *Q. J. R. Meteorol. Soc.*, *128*(585), 2187–2203.
Woodgate, R. A., and K. Aagaard (2005), Revising the Bering Strait freshwater flux into the Arctic Ocean, *Geophys. Res. Lett.*, *32*, L02602, doi:10.1029/2004GL021747.
Yankovsky, A. E., R. W. Garvine, and A. Münchow (2000), Mesoscale currents on the inner New Jersey shelf driven by the interaction of buoyancy and wind forcing, *J. Phys. Oceanogr.*, *30*(9), 2214–2230.

H. L. Johnson, Department of Earth Sciences, University of Oxford, Parks Road, Oxford, OX13PR, UK.
H. Melling, Institute of Ocean Sciences, PO Box 6000, Sidney, BC, V8L4B2 Canada.
A. Münchow and B. Rabe, College of Earth, Ocean, and Environment, University of Delaware, Robinson Hall, Newark, DE 19716, USA. (brabe@udel.edu)